Journal of Alloys and Compounds 1016 (2025) 178838

Contents lists available at ScienceDirect

Journal of Alloys and Compounds

journal homepage: www.elsevier.com/locate/jalcom

Highly tuneable icosahedral orders in complex Al-Pd-W-Fe alloys

Makito Aoyama [a], Satoshi Ohhashi [a], Hiroyuki Takakura [b], Yutaka Iwasaki [c], Nobuhisa Fujita [a,*]

[a] Institute of Multidisciplinary Research for Advanced Materials, Tohoku University, Sendai 980-8577, Japan
[b] Division of Applied Physics, Faculty of Engineering, Hokkaido University, Sapporo 060-8628, Japan
[c] National Institute for Materials Science, Tsukuba 305-0047, Japan

ARTICLE INFO

Keywords:
Icosahedral quasicrystals
Periodic approximants
Structural phase transition
Pseudogap
Electrical conductivity
Thermoelectric

ABSTRACT

We report the formation of novel complex intermetallics in Al-Pd-W-Fe alloys with varying icosahedral orders. The quaternary system is akin to the Al-Pd-Cr-Fe and Al-Pd-Mo-Fe systems, in which high-order periodic approximants associated with the face-centred icosahedral quasicrystal, i-$Al_{70}Pd_{20}Mn_{10}$, have been previously reported. Herein, an analogous high-order periodic approximant is identified at compositions of $Al_{67-68}Pd_{24}W_{1-2}Fe_{6-9}$, along with an icosahedral quasicrystal at approximately $Al_{69}Pd_{22}W_3Fe_6$. For the periodic approximant, millimetre-sized single grains were successfully obtained through slow cooling method combined with a post isothermal treatment at a sub-melting temperature. To our surprise, single grains annealed at 1223 K and 1248 K showed different crystal symmetries, suggesting a structural phase transition analogous to one observed in the corresponding approximant of the $Al_{70}Pd_{21}Mo_1Fe_8$ alloy. High-quality monophase samples of all three phases, with varying icosahedral orders, were obtained using several heuristic approaches. These monophase samples were finally subjected to a comparative assessment of their thermoelectric properties, which reveal contrasting behaviour associated with the position and shape of the pseudogap at the Fermi level.

1. Introduction

Since the first discovery of icosahedral quasicrystals (iQCs) in 1984 [1,2], the number of solid-state materials in this category has continued to grow. Intense research efforts have been invested to reveal their exceptional structural orders (see a recent review in Ref. [3] and references cited therein) and unusual physical properties [4], as well as in addressing the ongoing controversy regarding the structural stability of these and related materials [5–11]. More recently, interest in iQCs has been renewed by the observation of intriguing low-temperature quantum phenomena, such as anomalous quantum critical phenomena [12,13], superconductivity [14,15], and long-range magnetic orders [16,17].

It is widely believed that iQCs are cluster-based compounds, and there exist at least three distinct families of iQCs, each characterized by its constituent clusters [3]. For instance, face-centred iQCs found in Al-based alloys are based on Mackay-type clusters, whereas primitive as well as face-centred iQCs found in (Zn,Mg)-based alloys are based on Bergman clusters. The latest discovered family of primitive iQCs [18], based on Tsai clusters, has been attracting wide attention as they serve as a platform of various low-temperature phenomena [12,16]. All these families of iQCs are regarded as Hume-Rothery electronic compounds, each formed at a specific valence electron concentration [7,8].

Elucidating the structure of iQCs has remained an important challenge, as structural knowledge is crucial for understanding their unique physical properties. However, traditional crystallographic analyses are largely hindered by the absence of periodicity. In this respect, the highly accurate structural solution of the stable binary iQC, i-$YbCd_{5.7}$ [18], based on Tsai clusters, was a milestone achievement by Takakura et al. [19]. It demonstrated the effective incorporation of structural knowledge gained from periodic approximants (PAs) [20], including those of order 1/1 [21] and 2/1 [22], into the six-dimensional crystallographic modelling of the iQC.

PAs of an iQC are periodic crystals that share the same kinds of constituent clusters and their packing rules as the iQC. Each of the fundamental periods of the crystal structure is associated with an irreducible fraction, q/p, representing a rational approximant of the golden mean, $\tau = (1+\sqrt{5})/2$ [20]. Typically, q/p is a ratio of two successive Fibonacci numbers: 1/0, 1/1, 2/1, 3/2, 5/3, etc. For a cubic PA, a single q/p is sufficient to determine the fundamental periods in all three

* Corresponding author.
E-mail address: nobuhisa@tohoku.ac.jp (N. Fujita).

https://doi.org/10.1016/j.jallcom.2025.178838
Received 13 October 2024; Received in revised form 11 January 2025; Accepted 23 January 2025
Available online 26 January 2025

dimensions. The lattice parameter $a_{q/p}$ of a cubic q/p PA is related to the *quasilattice constant* a_R through $a_{q/p} = \frac{2(p+q\tau)}{\sqrt{2+\tau}} a_R$ [20], where a_R stands for the length of the six basis vectors (along fivefold axes) chosen such that the length of the six reciprocal basis vectors used to index the iQC's diffraction peaks is π/a_R [23,24]. Note that a_R defines the edge length of the three-dimensional tiling composed of two kinds of rhombohedra [25–27], employed as the underlying quasilattice of an iQC. In general, the higher the orders of periodic approximation, the larger the size of the unit cell, making the structure more like the iQC. The similarity is reflected in the chemical composition and, consequently, the valence electron concentration, or e/a ratio. Therefore, high-order PAs offer valuable insights into the structure and stability of iQCs.

The thermodynamically stable iQCs in the Al-Pd-TM (TM = Mn, Re, Ru, Os) systems [28,29], based on pseudo-Mackay clusters [3], have been attracting wide attention due to their potential feasibility for applications [30,31]. Despite previous studies, however, their atomic structure largely remains elusive. Structural investigations of PAs, especially high-order ones, are essential for gaining valuable insights into the problem. In the Al-Pd-TM (TM = Fe, Ru, Rh, Ir) systems, a few variants of 1/0 PAs, named the C, C_1, C_2, and C_3 phases, were reported in the literature [32–37]. More recently, a higher-order PA was discovered in an alloy with similar composition to C_1-AlPdFe but with a minor substitution of Fe with either Cr [38] or Mo [39]. The latter PA, belonging to the space group $Pa\bar{3}$ and having a lattice parameter of approximately 40 Å, can be considered a $2 \times 2 \times 2$ superstructure of the conventional cubic 2/1 PA [40].

Crystal structure refinement showed that the new 2/1 PA with the doubled supercell contains two kinds of constituent clusters [38]: the pseudo-Mackay cluster (pMC) and the mini-Bergman cluster (mBC), both of which have diameters of ~8Å. These clusters were spatially arranged such that their centres define the vertices of a three-dimensional tiling composed of four kinds of polyhedral cells called the *canonical cells* [3,41]. This tiling can be regarded as a $2 \times 2 \times 2$ superstructure of the standard 3/2 cubic approximant tiling (called the 3/2 cubic packing [41]) and is hereafter referred to as the $2^3{\cdot}3/2$ cubic packing. It was further noted that the arrangement of pMCs and mBCs exhibits a specific ordering, wherein pMCs occupy vertices of even parity while mBCs occupy vertices of odd parity [38]. Here, the parity of each vertex is defined as that of the sum of six integers used to index it. It is important to note that this specific type of ordering may naturally extend to that in face-centred (or F-type) iQCs [42–45]. The PA may now be called a $2^3{\cdot}3/2$ PA (instead of $2^3{\cdot}2/1$ PA) based on the cluster packing concept. Similarly, the C, C_1, C_2, and C_3 phases may now be referred to as 1/1 (rather than 1/0) PAs, with or without a $2 \times 2 \times 2$ superstructure. The present argument implies that the proper quasilattice constant a_R associated with the cluster packing is $1/\tau$ times the conventional one used to describe P-type Al-based iQCs [46]. Notably, a new six-dimensional structural model for F-type iQCs has recently been proposed, based on this understanding [47].

The $2^3{\cdot}3/2$ PAs [38,39] were found to exhibit a deep pseudogap near the Fermi energy [48], a characteristic often observed in quasicrystal-related materials [49]. While the conventional Hume-Rothery type argument asserts that such a pseudogap originates from the interaction between the Fermi sphere and (pseudo-)Brillouin-zone boundaries, it has been suggested that orbital hybridization plays a significant role in deepening it [50,51]. Indeed, it is considered that the hybridization between Al-*sp* and Cr/Mo-*d* orbitals is responsible for the depth variation of the pseudogaps in the two PAs [48].

Whether the pseudogap can be deepened further by selecting an element with stronger hybridization is worth examining. Tungsten (W) is considered a promising candidate because it not only shares similarities with Cr and Mo, but it could also enhance hybridization due to the more extended nature of its outer *d* orbitals. It is also worth noting that, in early metallurgical studies of iQC-related alloys, W was identified as one of the transition metals capable of promoting iQC formation when combined with Al and Fe [52]. The rationale behind the formation of the metastable Al-Fe-W iQC may be linked to the affinity of W for local icosahedral coordination. However, as in Refs. [38,39], the present study focuses more on the potential role of W in optimizing the electron concentration to stabilize a high-order PA or iQC electronically, when W is used as a minor replacement for Fe in C_1-AlPdFe.

We hereby report that, in the Al-Pd-W-Fe system, $2^3{\cdot}3/2$ PA and iQC phases can indeed be stabilized at suitable choices of composition. Additionally, a structural trend is uncovered as the amount of W is increased: The $2^3{\cdot}3/2$ PA is dominant within a compositional range of $Al_{67-68}Pd_{23-24}W_{1-2}Fe_{7-9}$, which will be replaced by the iQC as the W content is increased up to 3 at%. A similar trend was already suggested when Cr was used to substitute Fe [38]. Moreover, at $Al_{68}Pd_{24}W_1Fe_7$, we observed a structural phase transition at ~ 1223 K, from the $2^3{\cdot}3/2$ PA at higher temperatures to another form of 3/2 PA, analogous to the low-temperature variant with the trigonal space group $P\bar{3}$ reported below ~1023 K in the Al-Pd-Mo-Fe system [39].

The impact of these structural variations on the valence band structure, particularly on the pseudogap near the Fermi level, is revealed through thermoelectric measurements of the distinct compounds studied. Highly pure, monophase samples necessary for these measurements are made available through adjusting the composition and temperature, as confirmed using electron and powder X-ray diffraction. Additionally, slow cooling of the melt, combined with an extended post-annealing at sub-melting temperatures, proves successful in yielding high-quality single grains suitable for structure analysis.

2. Experimental

2.1. Sample synthesis

High-purity Al (99.99 %), Pd (99.9 %), W (99.9 %) and Fe (99.99 %) were used as the starting materials. The pure metals were weighed to achieve a total composition of $Al_{70}Pd_{21}W_xFe_{9-x}$ with x ranging from 1 to 7. The materials were then melted together using arc melting under Ar atmosphere in a two-step process: first, Pd, Fe, and W were melted together, followed by remelting the resulting alloy ingot with the remaining Al. This two-step process was designed to suppress Al evaporation and prevent the formation of phases with significantly higher melting temperatures than the target phases. However, the as-synthesized ingots still consisted of mixed phases. Therefore, annealing was an essential next step in our synthesis to improve alloy homogenization and promote the formation of the target phases.

Isothermal annealing was performed at temperatures ranging from 1073 to 1373 K. Fragmented pieces of the as-synthesized ingot were placed in an alumina (Al_2O_3) crucible, which was then sealed in a quartz tube under an Ar atmosphere to prevent oxidation during heat treatment. Heat treatment was conducted to promote homogenization and the formation of the target phases, using an electric furnace (Yamato, Muffle Furnace FO200) with various temperature programs. After isothermal annealing at elevated temperatures, the sample was cooled to room temperature via furnace cooling, unless otherwise stated (e.g., in the case of water quenching).

2.2. Characterization

Phase identification was conducted using powder X-ray diffraction (PW-XRD) (Ultima IV; Rigaku) with CuKα radiation (λ = 1.5406 Å). The Le Bail method [53] was applied to powder diffraction data from selected samples to index the diffraction peaks and estimate the lattice parameters using the JANA2020 software suite [54]. A scanning electron microscope (SEM) (SU6600, operating at an acceleration voltage of 15 kV; Hitachi) implementing an energy dispersive X-ray (EDX) spectrometer (INCA X-Act; Oxford Instruments) was used to acquire metallographic images to discern constituent phases and their estimated

compositions. SEM observations were conducted on either polished flat surfaces of polycrystalline samples or cleavage surfaces of single crystalline samples, using secondary-electron (SE) mode or backscattered-electron (BSE) mode. To find better estimates of the compositions, an electron-probe micro-analyzer (EPMA) (JXA-8530F, operating at an acceleration voltage of 15 kV; JEOL) using wavelength dispersive X-ray (WDX) spectroscopy was employed. A transmission electron microscope (TEM) (JEM-2000EXII, operating at an acceleration voltage of 200 kV; JEOL) was utilized to acquire crystallographic information of individual phases in the samples. For TEM experiments, an alloy sample was first ground into a fine powder in a small amount of ethanol and then dispersed onto a Cu grid. Single-crystal X-ray diffraction (SC-XRD) measurements were performed on single crystal specimens (~50 μm) of the two variants of 3/2 PA, using an XtaLAB Synergy-R single-crystal diffractometer equipped with Hybrid Pixel Array Detector (HyPix6000; Rigaku) with Mo Kα radiation (λ = 0.71073 Å). The CrysAlis^{Pro} software Ver.42.49 (Rigaku Oxford Diffraction) was used for the indexing of Bragg peaks and integration of peak intensities, where automatic absorption correction was applied.

2.3. Measurements of thermoelectric properties

For measuring thermoelectric properties, dense disc-shaped bulk samples were obtained by placing powdered samples, ground in a mortar, into a graphite die with an inner diameter of 10 mm, followed by spark plasma sintering (LABOX-110MC; SinterLand, Inc., Niigata, Japan) in a purified argon atmosphere. The applied pressure and temperature during the sintering process were adjusted up to 90 MPa and 1163 K, respectively. The electrical conductivity (σ) and Seebeck coefficient (S) of these samples were measured from 300 K to 873 K using the four-probe method and steady-state temperature gradient method, respectively (ZEM-3; Advance Riko, Inc., Kanagawa, Japan). For

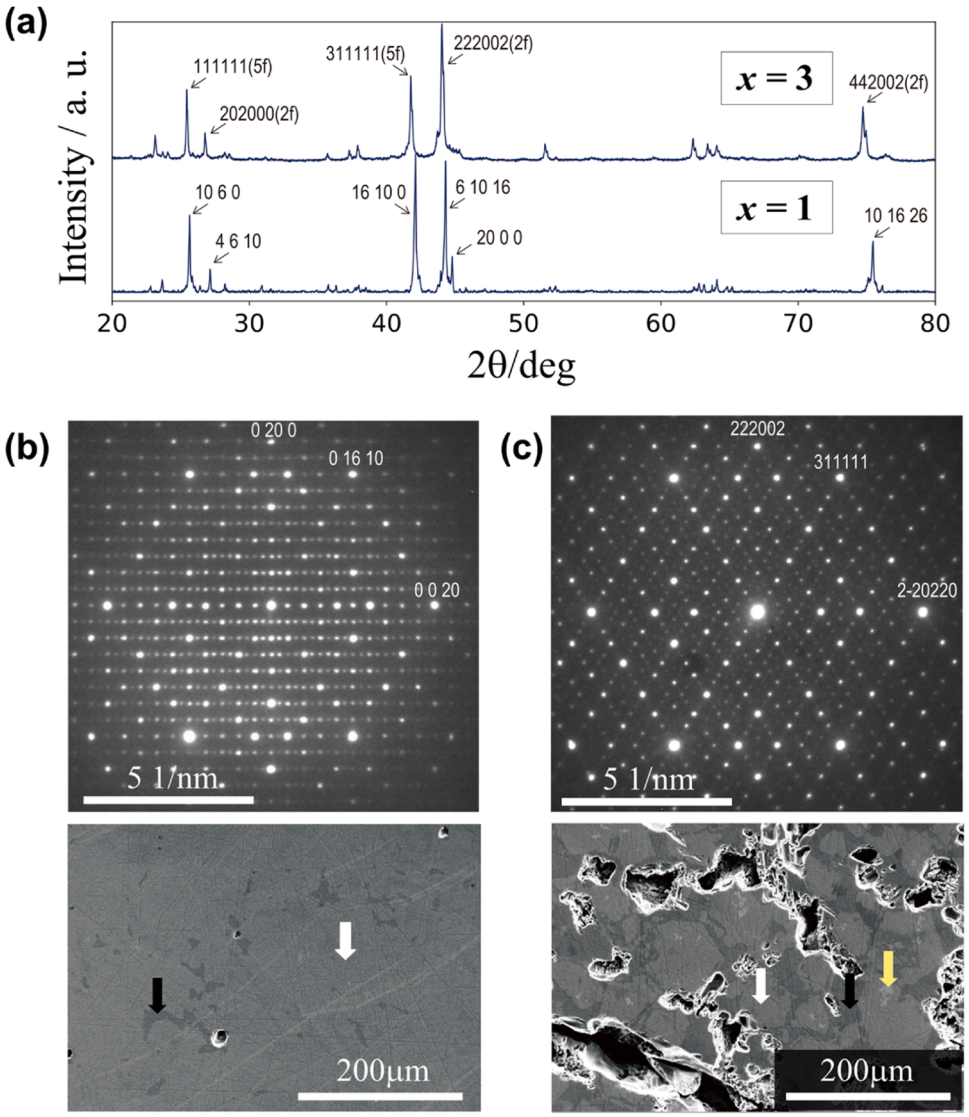

Fig. 1. (a) PW-XRD (Cu-Kα) patterns taken from $Al_{70}Pd_{21}W_xFe_{9-x}$ ($x = 1$ and 3) alloys annealed at 1173 K for 7 days. Prominent peaks are tentatively indexed assuming a cubic 2^3 superstructure of 3/2 PA for $x = 1$ and an F-type iQC for $x = 3$. (b) (top) A selected area diffraction pattern taken from the $x = 1$ sample with the incidence along <100>, indicating the formation of the $2^3{\cdot}3/2$ PA with space group $Pa\bar{3}$. Peaks are indexed accordingly. (bottom) An SEM micrograph (SE mode) of the $x = 1$ sample (polished surface). Estimated compositions from SEM-EDX analysis are as follows: $Al_{67.8}Pd_{23.5}W_{0.9}Fe_{7.8}$ for the major light-grey areas (white arrowhead) and $Al_{71.5}Pd_{20.7}W_{0.1}Fe_{7.7}$ for the remaining darker areas (black arrowhead). (c) (top) A selected area diffraction pattern taken from the $x = 3$ sample with the incidence along a twofold axis, indicating the formation of an F-type iQC. (bottom) An SEM micrograph (SE mode) of the $x = 3$ sample (polished surface). Estimated compositions from SEM-EDX analysis are as follows: $Al_{76.6}Pd_{0.6}W_{22.1}Fe_{0.8}$ for the fine granular regions with the brightest contrast (yellow arrow), $Al_{67.2}Pd_{24.6}W_{2.7}Fe_{5.5}$ for the surrounding light-grey areas (white arrow), and $Al_{71.3}Pd_{21.9}W_{0.3}Fe_{6.6}$ for the darkest areas (black arrow).

evaluating the dimensionless figure of merit, zT, thermal conductivity (κ) was measured using the laser flash method (LFA, TC-7000, Advance Riko, Inc.).

3. Results and discussion

3.1. An initial scan of the compositional space

Four alloy samples with nominal compositions, $Al_{70}Pd_{21}W_xFe_{9-x}$ ($x = 1, 3, 5, 7$), were initially prepared to gather preliminary data on the potential formation of complex intermetallic compounds. The compositions of Al and Pd were chosen based on the reference composition, $Al_{70}Pd_{21}Mo_1Fe_8$, of the $2^3{\cdot}3/2$ PA in the Al-Pd-Mo-Fe system [39]. Isothermal annealing was conducted at 1173 K for a week.

The PW-XRD pattern obtained from the $x = 1$ sample, shown in Fig. 1(a), exhibits similar features to the $2^3{\cdot}3/2$ PAs in the Al-Pd-Cr-Fe and Al-Pd-Mo-Fe systems [38,39]. These features include the two prominent peaks at $2\theta \sim 42^\circ$ and 44° (indexed as {16,10,0} and {6,10, 16}, respectively), accompanied by a minor peak around $2\theta \sim 45^\circ$ (indexed as {20,0,0}). The pattern could be fitted with an estimated lattice parameter of $a = 2a_{3/2} \sim 40.4$Å. The formation of the $2^3{\cdot}3/2$ PA is also evident in the electron diffraction pattern shown in Fig. 1(b), top, which compares well with Fig. 3(a) of Ref. [38]. In the SEM image of the $x = 1$ sample (Fig. 1(b), bottom), two distinct phases are noticeable, depicted as light grey and dark grey areas. An estimated composition (via SEM-EDX) of the light-grey areas was $Al_{\sim 67}Pd_{\sim 24}W_{\sim 1}Fe_{\sim 8}$, which fairly agrees with the nominal composition, thus likely representing the target phase. On the contrary, the dark-grey areas had an estimated composition of $Al_{\sim 72}Pd_{\sim 20}W_{\sim 0}Fe_{\sim 8}$, apparently deficient in W. The latter may represent a quaternary extension of ε-AlPdFe [32]. A few micro-voids can be observed attached to the latter phase. Note that the PW-XRD profile of the $x = 1$ sample (Fig. 1(a); see also Fig. 2(a)) also suggests a potential inclusion of the C_1 phase, which, however, was not observed in the SEM image (Fig. 1(b), bottom).

The PW-XRD pattern of the $x = 3$ sample (Fig. 1(a)) appears to indicate the formation of an F-type iQC phase, analogous to i-Al-Pd-Mn [28]. Diffraction peaks are thus indexed by six even or six odd integers, with a fitted quasilattice constant of $a_F = 2a_R \sim 5.65$ Å. Additional evidence is provided by electron diffraction along twofold direction, as shown in Fig. 1(c), top, which demonstrates the τ-scaling characteristic of an F-type iQC [42]. In the SEM image of the $x = 3$ sample (Fig. 1(c), bottom), the majority phase is shown as light-grey areas, with an estimated composition (SEM-EDX) of $Al_{\sim 67}Pd_{\sim 24}W_{\sim 3}Fe_{\sim 6}$, which is consistent with the nominal composition and thus likely representing the iQC phase. The minority phase with dark-grey contrast is again W deficient, with an estimated composition of $Al_{\sim 71}Pd_{\sim 22}W_{\sim 0}Fe_{\sim 7}$, likely representing a quaternary extension of ε-AlPdFe [32]. It is worth noting that the current sample contains large voids with diameters exceeding 100 μm, exhibiting significantly enhanced porosity compared to the sample with a lower W content ($x = 1$). The same trend is indeed commonly observed in other samples, as will be presented below.

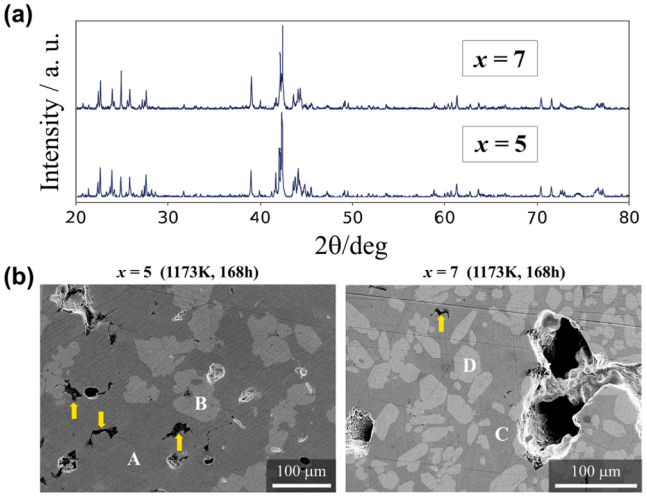

Fig. 2. (a) PW-XRD (Cu-Kα) patterns taken from $Al_{70}Pd_{21}W_xFe_{9-x}$ ($x = 5$ and 7) alloys annealed at 1173 K for 7 days. (b) SEM micrographs (SE mode) taken from the two samples. Each sample exhibits two primary phases with different gray levels. Estimated compositions of these phases as determined by SEM-EDX analysis are A: $Al_{72.1}Pd_{23.1}W_{0.5}Fe_{4.3}$, B: $Al_{71.3}Pd_{16.9}W_{11.3}Fe_{0.6}$, C: $Al_{72.3}Pd_{24.5}W_{0.6}Fe_{2.6}$, and D: $Al_{71.3}Pd_{16.8}W_{11.6}Fe_{0.3}$. Yellow arrows indicate the remains of Al-flux.

The other two samples (with $x = 5$ and 7) exhibit similar PW-XRD patterns (Fig. 2(a)) without any indications of iQC or PA. SEM micrographs in Fig. 2(b) reveal the coexistence of two primary phases in these samples: one rich in W and the other poor in W. Based on their estimated compositions, the W-poor phase appears to be the ε phase [32], while the W-rich phase does not appear to be reported in the literature. Therefore, we synthesized another sample with a nominal composition of $Al_{71.3}Pd_{16.7}W_{11.6}Fe_{0.4}$, annealed at 1223 K for 240 hours, to find if it primarily consisted of the W-rich phase. An SEM micrograph (not shown) revealed that the sample again consisted of two similar phases, with the W-rich phase occupying roughly 90 % of the total volume. A PW-XRD pattern obtained from the sample is presented in Supplementary Fig. 1 alongside a simulated pattern for a model of ε_6-AlPdMn [55], employed as a reference to the ε-phase structural family. Note the qualitative agreement between the superposition of the two patterns and the observed patterns from the mixed-phase samples in Fig. 2(a). We have also managed to collect SC-XRD data from a fine mono-grain cut out from the $Al_{71.3}Pd_{16.7}W_{11.6}Fe_{0.4}$ sample. The resulting dataset allowed us to solve the crystal structure, which was determined to be hexagonal with space group $P6_3/m$ and lattice parameters $a = 11.36$ Å and $c = 12.99$ Å. The details of the structural analysis will be presented elsewhere.

We also investigated the effects of annealing temperature on the quality of samples with compositions of $x = 1$ and $x = 3$. Fig. 3(a) and (b) compare PW-XRD patterns taken from samples annealed at temperatures ranging from 1073 K and 1373 K; to expedite the search, the data for 1173 K are reproduced from Fig. 1(a). At 1073 K, moderate atomic diffusion appears insufficient for homogenization, resulting in a dominant portion of impurities remaining in the $x = 1$ sample. As indicated in Fig. 3(a), these impurities are mostly attributable to the C_1 phase, with an estimated lattice constant of $a \equiv 2a_{1/1} \sim 15.4$Å at 1073 K, which likely resulted from the arc melting process. In contrast, the C_1 phase is not observed in the $x = 3$ sample. The peaks corresponding to the target phases, PA (for $x = 1$) and iQC (for $x = 3$), remain broad at this stage.

The quality of the samples, as indicated by peak sharpness and the suppression of impurities, is enhanced at higher temperatures, e.g., at 1223 K for $x = 1$ and 1223 K or 1258 K for $x = 3$. In Fig. 3(a), the PW-XRD pattern of the $x = 1$ alloy annealed at 1223 K is indexed as the $2^3{\cdot}3/2$ PA, with an estimated lattice parameter of $a = 2a_{3/2} \sim 40.5$Å. In this pattern, a trace of the C_1 phase can still be noticed. The corresponding SEM image in Fig. 3(c) reveals a millimeter-sized monophase region of the target compound with enhanced homogeneity as compared to that in the sample annealed at 1173 K for 7 days (Fig. 1(b), bottom). A small lighter-grey region shows minor inclusion of a W-richer component, which was undetected in the PW-XRD data. As we will see in a later section, the C_1 phase can be largely suppressed by prolonged annealing. As for the $x = 3$ alloys annealed at 1223 K, the PW-XRD pattern can be well fitted as an F-type iQC with an estimated quasilattice constant of $a_F = 2a_R \sim 5.65$Å, with no visible impurity peaks. However, the SEM image in Fig. 3(d) reveals the presence of a tiny amount of additional components, both W-richer and W-poorer, which can still be suppressed by prolonged annealing.

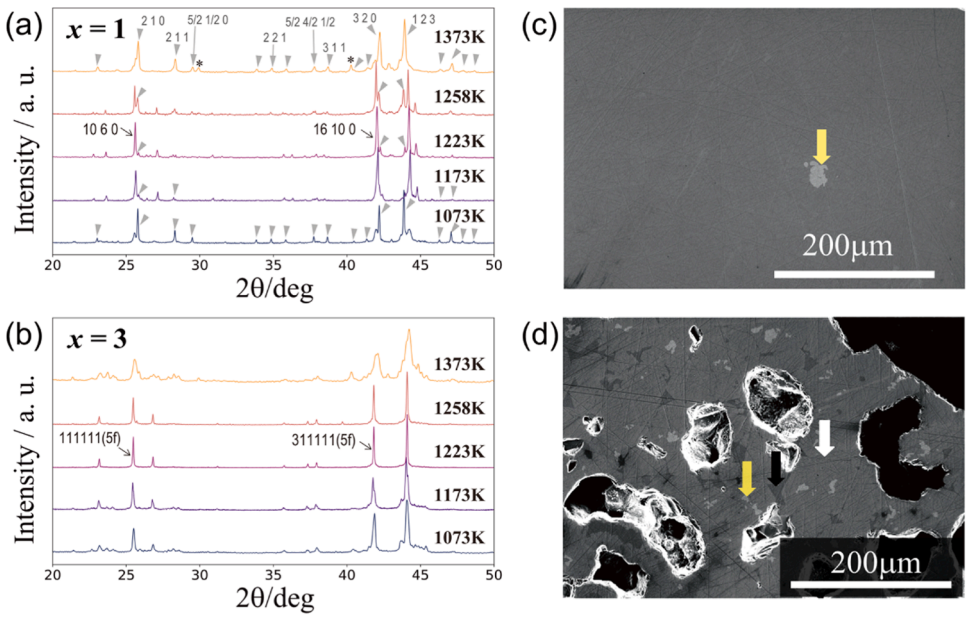

Fig. 3. (a and b) PW-XRD (Cu-Kα) patterns of samples with compositions $x = 1$ and $x = 3$, respectively, annealed at 1073, 1173, 1223, 1258, and 1373 K. The annealing time was 5 days except that the data for 1173 K are reproduced from Fig. 1(a). In (a), the expected peak positions for the C_1 phase are indicated using gray arrowhead, whereas peaks marked with asterisks may be assigned to the β phase (~ 30°) and elemental W (~ 40°). Peaks are indexed for the $2^3{\cdot}3/2$ PA (a, 1223 K), F-type iQC (b, 1223 K), and C_1 phase (a, 1373 K). (c and d) SEM images, taken in the SE mode, of the samples with compositions $x = 1$ and $x = 3$, respectively, which were annealed at 1223 K for 5 days. Estimated compositions from SEM-EDX analysis are as follows: (c) $Al_{67.1}Pd_{23.8}W_{1.0}Fe_{8.1}$ for the majority phase (light-grey areas) and $Al_{62.9}Pd_{18.4}W_{18.3}Fe_{0.5}$ for the small area with brighter contrast (yellow arrow). (d) $Al_{76.6}Pd_{0.7}W_{22.0}Fe_{0.8}$ for the fine granular regions with the brightest contrast (yellow arrow), $Al_{68.2}Pd_{23.3}W_{2.9}Fe_{5.7}$ for the majority phase (light-grey areas indicated with white arrow), and $Al_{71.4}Pd_{22.5}W_{0.5}Fe_{5.6}$ for the remaining darkest areas (black arrow).

The $x = 1$ alloy annealed at 1373 K shows that the PA phase was fully decomposed, leading to the reemergence of the C_1 phase, which is stable at higher temperatures; see Fig. 3(a). In contrast, the $x = 3$ alloy annealed at 1373 K may have liquefied without leaving any trace of the C_1 phase (Fig. 3(b)).

3.2. Synthesis of single-grained samples

We hereby present our attempts to synthesize single-grained samples of the 3/2 PA and iQC phases, with the primary goal of obtaining a high-quality single crystal specimen suitable for structural analysis. In fact, this gave us useful insights into their phase formation behaviors near the melting temperatures. As previously, our initial compositions were $x = 1$ and $x = 3$. The melting step was conducted at 1433 K for 2 days to ensure a fully homogenized liquid. Subsequently, the samples were slowly cooled at a rate of 5 K per hour to 1223 K, at which point they were annealed for 10 days. Both samples exhibited a metallic luster, though no clear facets were visible.

The PW-XRD pattern in Fig. 4, top, reveals a prominent signature of the C_1 phase at $x = 1$, despite prolonged annealing at a sub-melting temperature. This suggests that the C_1 phase is the initial crystallizing phase during the cooling process and exhibits high stability under solid-state reaction conditions, thereby impeding atomic diffusion. In contrast, the primary phases of the $x = 3$ sample are the 3/2 PA and iQC phases, with no sign of the C_1 phase. Prolonged annealing proved relatively easy to suppress the 3/2 PA component in this sample.

We thus employed an alloy composition of $x = 2$ for the next synthesis, under the assumption that increasing the W content would destabilize the C_1 phase and thereby avoid its formation. We used the same melting and cooling processes as before, but the final isothermal annealing at 1223 K was shortened to 5 days. A PW-XRD pattern taken from a fragment of the sample is shown in Fig. 4(a), the third row, which confirms that the material is predominantly the 3/2 PA. A facet plane was also visible on the surface of the entire sample (Fig. 4(b), top),

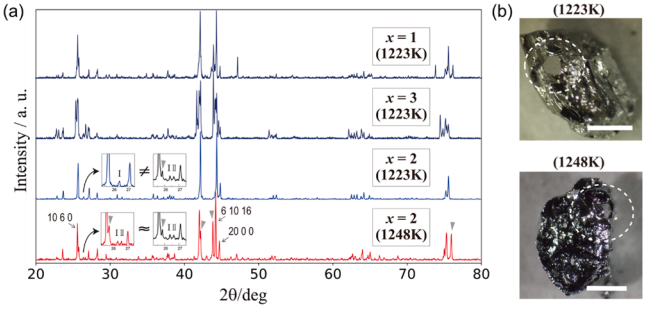

Fig. 4. (a) PW-XRD (Cu-Kα) patterns taken from four samples obtained via slow-cooling method. The weighing composition as well as the temperature of the final isothermal step is indicated for each pattern. Minor peaks indexed {0 0 12}(= I) and {7 7 7}(= II) for the $2^3{\cdot}3/2$ PA are highlighted in the insets for the two $x = 2$ samples. The corresponding section of the $x = 1$ data in Fig. 3(a), third row, is shown in black colour for comparison. The peak labelled II, which is associated with the doubling of the unit cell, is absent in the third row, indicating the formation of the trigonal variant of 3/2 PA. Grey arrowheads are used to indicate noticeable impurity peaks due to the inclusion of the C_1 phase. (b) Photographs showing the outer appearance of the $x = 2$ samples, annealed at 1223 K and 1248 K. The scale bars correspond to 1 mm. A facet plane can be seen in the center of dashed circle.

suggesting that fine single grains were obtained. The composition of the single grains was estimated to be $Al_{67.8}Pd_{23.2}W_{1.0}Fe_{8.0}$ using EPMA-WDX, indicating a depletion of W from the initial weighing composition, $Al_{70}Pd_{21}W_2Fe_7$.

As clarified in the insets of Fig. 4(a), third row, a minor difference from the cubic $2^3{\cdot}3/2$ PA can be recognized within $26° < 2\theta < 27°$, where we find a peak associated with the doubling of the unit cell is missing. This reminded us of the trigonal variant of the 3/2 PA observed in the Al-Pd-Mo-Fe system, for which similar difference in PW-XRD from the cubic $2^3{\cdot}3/2$ PA was observed. In the latter system, a reversible

structural phase transition was reported at approximately 1023 K from the $2^3{\cdot}3/2$ PA (high-temperature phase) to the trigonal variant (low-temperature phase) [39], without a measurable change in the composition of approximately $Al_{70}Pd_{21}Mo_1Fe_8$. In contrast, the corresponding feature of the PW-XRD profile taken from the $x = 1$ sample isothermally annealed at 1223 K for 5 days (Fig. 3(a), third raw) shows a double-peak structure characteristic of the cubic $2^3{\cdot}3/2$ PA. Intriguingly, different variants were obtained despite the same annealing temperature of 1223 K for both samples (isothermal or isothermal after slow cooling from the melt). The estimated compositions were also rather similar: $Al_{67.1}Pd_{23.8}W_{1.0}Fe_{8.1}$ (SEM-EDX) for the isothermal sample and $Al_{67.8}Pd_{23.2}W_{1.0}Fe_{8.0}$ (EPMA-WDX) for the single grained sample. The discrepancy between the two samples will be addressed in more detail in the next section.

To obtain single grains of the cubic $2^3{\cdot}3/2$ PA, we conducted another synthesis with the same $x = 2$ composition, raising the final annealing temperature to 1248 K. Fig. 4(a), the fourth row, shows a PW-XRD pattern taken from the resulting sample, indicating that the $2^3{\cdot}3/2$ PA was indeed obtained along with the C_1 phase as the secondary phase. This sample also exhibited a visible facet plane, as seen in Fig. 4(b). An estimated composition (EPMA-WDX) of the single grains, $Al_{67.6}Pd_{22.1}W_{1.3}Fe_{9.0}$, was slightly richer in W than the other single grained sample. This might explain the slight lattice expansion observed in the PW-XRD pattern. The coexistence of both the 3/2 PA and C_1 phases may have resulted from minor temperature variations in the furnace, if 1248 K were nearly at the peritectic point between C_1 + liquid and 3/2 PA or vice versa.

Tiny crystals, $\leq$ 50 μm in diameter, were extracted from both single-grained samples annealed at 1223 K and 1248 K and subjected to SC-XRD measurements (see Section 2.2 for the methodology). Primary two-dimensional sections of the diffraction intensity distribution in reciprocal space were reconstructed using CrysAlis^{Pro} software (Ver. 42.49) and shown in Fig. 5, in which the peak indexing was performed on the main reflections based on the basic 'cubic' unit cell of the 3/2 PA. The fitted lattice parameters of the basic 'cubic' Bravais lattice were $a_{3/2}$ = 20.23 Å (trigonal 3/2) and $a_{3/2}$= 20.24 Å (cubic $2^3{\cdot}3/2$).

The full reflection indexing of the high-temperature phase requires a 2^3 cubic supercell with a lattice parameter of $a = 2a_{3/2} = 40.48$ Å. The extinction rules for the $Pa\bar{3}$ space group are evident from the $hk0$ section [38,39]. As for the low-temperature phase, the superlattice reflections could be well-indexed with a trigonal supercell with lattice parameters of $a = b = 28.57$ Å, $c = 34.99$ Å, $\alpha = \beta = 90°$ and $\gamma = 120°$. Fig. 5(e) also suggests that the present crystal is twinned with four possible orientations for the threefold axis, parallel to the <111> directions of the basic unit cell. These features were also reported for the low-temperature trigonal variant in the Al-Pd-Mo-Fe system [39].

3.3. Synthesis of monophase samples

Monophase samples are crucial for comparative investigations of the physical properties of different intermetallic phases. Hence, this section aims to obtain monophase samples of the two variants of the 3/2 PA (cubic and trigonal) and iQC. One would generally expect that, starting from an appropriate weighing composition, prolonged isothermal annealing would enhance the purity of each phase.

Fig. 6 shows PW-XRD patterns and SEM micrographs of $x = 1$ and $x = 3$ alloys obtained through prolonged isothermal annealing at 1223 K, with annealing times being 25 days and 15 days, respectively.

The PW-XRD profile of the $x = 1$ sample (Fig. 6(a), top row) shows that the C_1 phase has almost completely vanished, in contrast to Fig. 3 (a), third row, which shows the PW-XRD profile of a sample with much shorter annealing. The pattern could be fitted as the cubic $2^3{\cdot}3/2$ PA with an estimated lattice parameter of $a = 2a_{3/2} \sim 40.5$Å. The SEM micrographs in Fig. 6(b) suggest that the current sample is a highly homogeneous single-phase alloy. However, tiny spots with darker contrast, accumulated at the periphery of the fragment, indicate a minor inclusion of residual C_1-phase components. Spherical micro-voids observed near the darker spots most likely resulted from vacancy condensation induced by the Kirkendall effect [56–58], driven by the significant difference in the diffusion rates between heavy (W) and light (Al/Fe) elements during annealing. These Kirkendall voids might be interpreted as remnants of W-deficient regions in the as-arc-melted ingot. In the following subsection (Section 3.4), the current sample is referred to as Sample-H_1, where 'H' stands for the higher-temperature

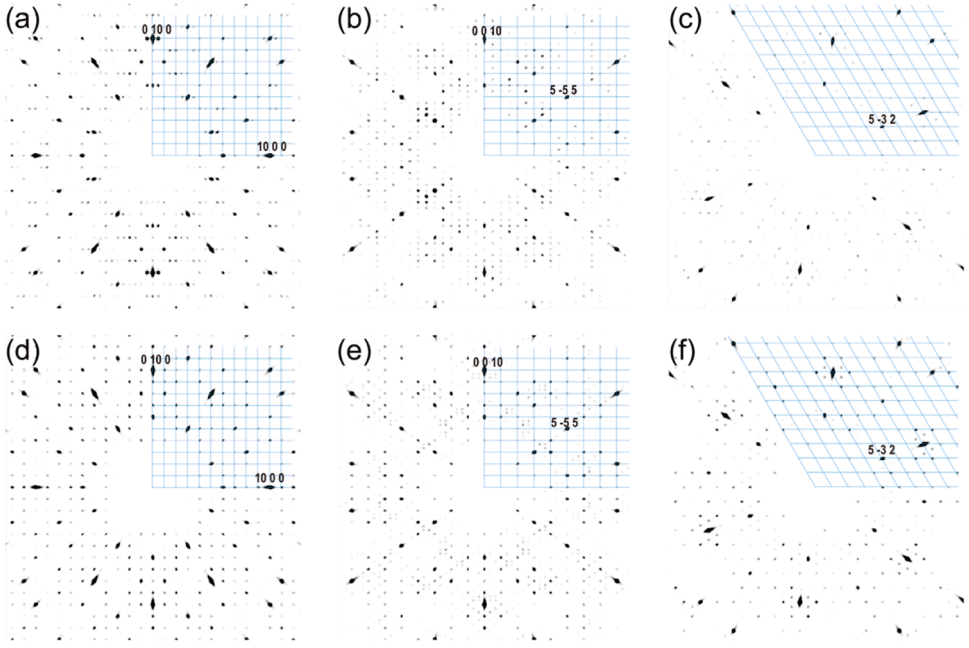

Fig. 5. Reconstructed reciprocal-space sections, which include the origin, of the SC-XRD datasets obtained from (a,b,c) a single-crystal specimen annealed at 1248 K and (d,e,f) one annealed at 1223 K. Light-blue grids are used as a reference for the reciprocal lattice of the basic Bravais lattice of the 3/2 PA, along with Miller indices for selected points. All panels, except (d), show superlattice reflections corresponding to the respective supercells. The twinning of the low-temperature phase is also evident from (e).

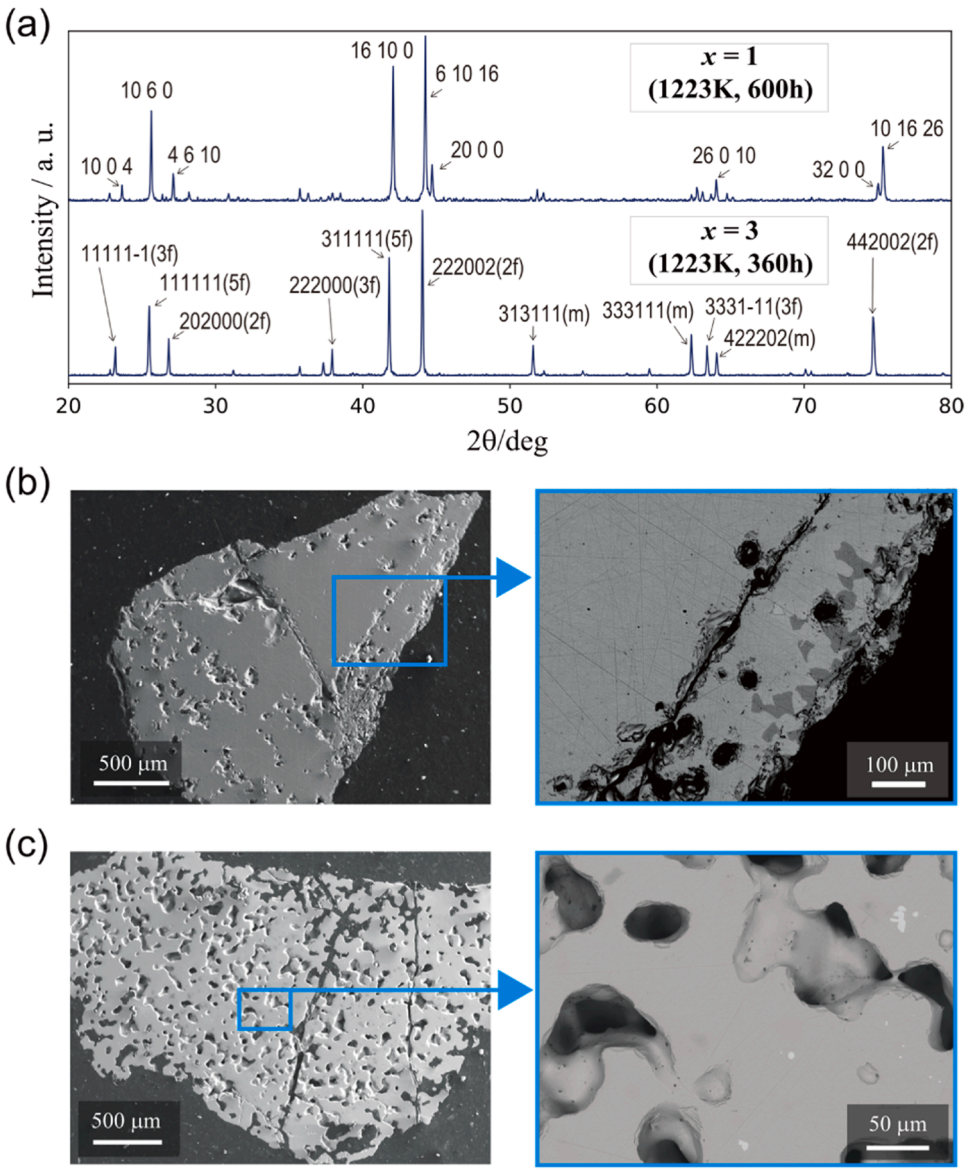

Fig. 6. (a) PW-XRD (Cu-Kα) patterns taken from $x = 1$ and $x = 3$ alloys obtained via prolonged isothermal annealing at 1223 K, conforming the high purity of the samples with the cubic $2^3{\cdot}3/2$ PA and iQC, respectively. Diffraction peaks are indexed accordingly. (b and c) SEM micrographs taken from polished sections of the $x = 1$ and $x = 3$ samples, respectively, in the SE mode (left) and BSE mode (right). Enlarged images on the right confirm the compositional homogeneity of both samples. Using EPMA-WDX, the compositions of the dominant phases are estimated to be $Al_{67.3}Pd_{23.2}W_{0.8}Fe_{8.7}$ in (b) and $Al_{69.2}Pd_{22.1}W_{2.9}Fe_{5.8}$ in (c). In (b), darker gray spots accumulating near the periphery are identified as the C_1 phase, with an estimated composition of $Al_{67.3}Pd_{21.6}W_{0.2}Fe_{10.9}$. In (c), tiny white dots within the iQC matrix are attributed to a residual W-rich component, with an estimated composition of $Al_{78.9}Pd_{0.5}W_{19.8}Fe_{0.8}$ being close to Al_4W.

cubic variant of the 3/2 PA and the subscript '1' for the nominal W concentration ($x = 1$).

Meanwhile, Fig. 6(a), bottom row, shows the PW-XRD profile of the $x = 3$ sample. The pattern could be fitted as an F-type iQC with an estimated quasilattice constant of $a_F = 2a_R \sim 5.66\AA$, without any significant peaks arising from extra phases as for the 5-day annealed sample shown in Fig. 3(b), third row. Furthermore, the corresponding backscattered electron image in Fig. 6(c) indicates that the homogeneity of the current sample is much higher than that of the sample shown in Fig. 3(d). The composition of this iQC phase was estimated to be $Al_{69.2}Pd_{22.1}W_{2.9}Fe_{5.8}$. Meanwhile, despite prolonged annealing, considerable porosity with large voids persisted throughout the sample. The irregular morphologies of these voids may be associated with the growth kinetics of the iQC phase, including phason-related dislocation motion. These voids could also be interpreted as remnants of W-deficient regions, likely comprising the ε-phase, within the as-arc-melted ingot. We note that the atomic number density of the ε-phase [55] is significantly lower, at approximately 85 % of that of the $2^3{\cdot}3/2$ PA [38], iQC or W-rich phases involved. The present sample will be referred to as Sample-Q_3 in Section3.4, where 'Q' stands for 'quasicrystal' and the subscript '3' for the nominal W concentration ($x = 3$). Incidentally, an almost negligible amount of an unwanted W-rich phase was observed within the iQC matrix.

To gain further insights into the phase formation behaviour of the two structural variants of 3/2 PA, an as-synthesized x = 2 alloy was subjected to isothermal annealing at 1223 K for 5 and 10 days without the melting process. This resulted in highly homogeneous alloys, showing the double-peak signature of the cubic $2^3{\cdot}3/2$ PA in the PW-XRD profiles (see Supplementary Fig. 2 for details). The 10-day annealed sample is referred to as Sample-H_2 in Section 3.4. The meaning of the subscript '2' is the same as before. It is worth noting that increasing the W content inhibits the formation of the C_1 phase, thereby

allowing for a high-quality monophase sample to be obtained in a shorter annealing time.

We have reached the stage of investigating how to obtain a high-quality monophase sample of the trigonal 3/2 PA. As described in Section 3.2, the trigonal variant was coincidentally identified in a single-grained sample obtained by melting an as-synthesized $x = 2$ alloy, then slowly cooling it down to 1223 K and holding it at that temperature for 5 days. Its estimated composition was close to the weighing composition of $x = 1$ used in this study. However, isothermal annealing of an as-synthesized $x = 1$ alloy at 1223 K, which best promotes atomic diffusion, always resulted in a sample exhibiting the double-peak signature of the cubic 2^3·3/2 PA in the PW-XRD profile, often accompanied by W-poorer (C_1 and/or ϵ) and W-richer impurities (see Figs. 3 and 6). Although prolonged annealing improved the purity of the main phase, a single-phase sample of the trigonal 3/2 PA was never obtained. We also observed that the primary phase tends to be slightly W-deficient, possibly due to the consumption of W by W-rich impurities. These W-rich phases with high melting temperatures may originate from arc-melted ingots but are not easily dissolved through solid-state reactions, leading to W deficiency relative to the nominal composition. We speculate that such a sample may also have slight compositional variations, potentially resulting in a mixture of the two structural variants, as the phase transition temperature likely depends on the actual alloy composition, particularly the W content. Therefore, achieving sufficient homogeneity in the resulting alloy seems essential to ensure a monophase sample of the trigonal 3/2 PA.

We hereby explore the potential advantage of the melting process before isothermal annealing to promote compositional homogeneity by allowing W-rich impurities to be dissolved more easily.

We used an as-synthesized $x = 1$ alloy as the starting material. First, the alloy was melted by holding it at 1433 K for 12 hours, followed by water-quenching to obtain a frozen liquid state. After polishing the outer surface of the quenched sample to remove an oxide layer, which resulted from the quenching process, fragments of the alloy were subjected to isothermal annealing at 1203 K for either 5 or 10 days. PW-XRD patterns and SEM micrographs shown in Fig. 7 confirm that the samples are highly homogeneous. Micro-voids are uniformly distributed throughout the samples. A minor inclusion of an unwanted W-rich component is observed at the periphery of the sample annealed for 5 days, but it is absent in the sample annealed for 10 days. In Section3.4, the latter sample will be referred to as Sample-L_1, where 'L' stands for the lower-temperature variant of the 3/2 PA. The meaning of the subscript '1' is the same as before. Most importantly, the single-peak signature of the trigonal 3/2 PA near $2\theta \approx 26.4^\circ$ is clearly visible in both PW-XRD profiles.

As demonstrated above, we have successfully obtained high-quality monophase samples of the cubic and trigonal variants of the 3/2 PA, which are connected through a structural phase transition, as well as the iQC. While the iQC sample was achieved with a starting composition of $x = 3$, either variant of the 3/2 PA can be realized with both $x = 1$ and $x = 2$, provided that a suitable annealing process is applied. Note that different temperature profiles (with and without pre-melting followed by rapid cooling, or different isothermal annealing temperatures) applied to an $x = 1$ alloy led to the formation of two distinct variants.

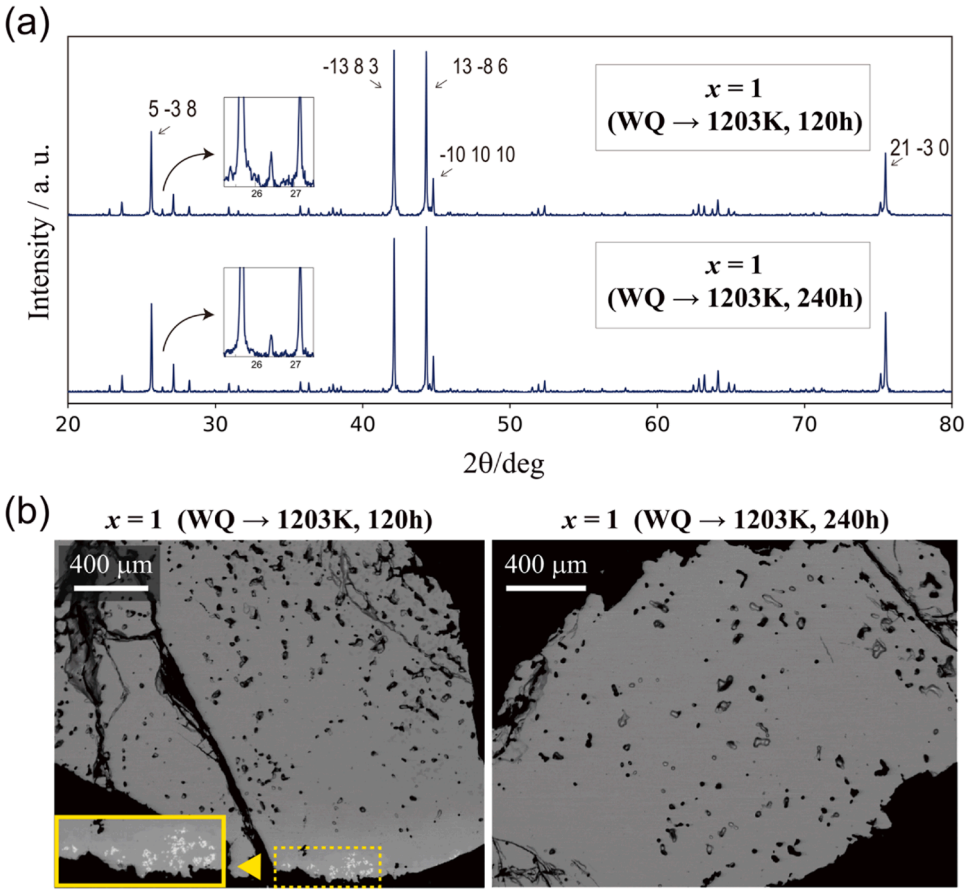

Fig. 7. (a) PW-XRD (Cu-Kα) patterns and (b) SEM micrographs (BSE mode) taken from the samples annealed at 1203 K for 5 and 10 days after water-quenching a liquefied $x = 1$ alloy. In (a), the single-peak signature of the low temperature variant of 3/2 PA (trigonal phase) in both profiles within $26^\circ < 2\theta < 27^\circ$ is highlighted in the insets. Estimated compositions (EPMA-WDX) of the majority phase in both samples are $Al_{68.7}Pd_{22.0}W_{0.7}Fe_{8.6}$ and $Al_{68.4}Pd_{22.5}W_{0.7}Fe_{8.5}$, respectively. The inset of the left panel shows a magnified image of the region enclosed by the dashed box, highlighting the inclusion of a W-rich component (white spots), with an estimated composition of $Al_{65.7}Pd_{16.7}W_{16.9}Fe_{0.6}$ as determined by EPMA-WDX.

This may be due to that a slight variation in local composition arising from the thermal history of the alloy will most likely affect the transition temperature, which in the present case close to 950 °C. It is therefore crucial to ensure sufficient homogeneity to precisely determine the transition temperature at a given alloy composition. A more detailed investigation into this issue is currently underway, and the results will be presented elsewhere.

3.4. Thermoelectric properties

Here, we present thermoelectric measurements on highly homogeneous samples, aiming to probe potential differences arising from distinct icosahedral orders and varying W contents. Four high-quality monophase samples, obtained as described in the preceding subsection and summarized in Table 1, were used. The samples were first crushed into powder and then moulded into densified, button-shaped bulk forms using spark plasma sintering.

Fig. 8(a) presents the temperature dependence of electrical conductivity (σ), which gradually increases with rising temperature, confirming the non-metallic behaviour characteristic of iQCs and high order PAs. The presence of a deep pseudogap in their valence electronic structure [48–49] could be linked to the quantitative differences observed between the samples. Here we recall that the electrical conductivity from the Boltzmann transport equation can be written as [59]:

$$\sigma = e^2 \int \left(-\frac{\partial f}{\partial E} \right) \Sigma(E) dE,$$

where e is the elementary charge, and $f(E) := \left(1 + \exp(\frac{E-\mu}{k_B T})\right)^{-1}$ is the Fermi-Dirac distribution function with μ representing the chemical potential (or the Fermi energy at temperature T). $\Sigma(E)$ is known as the transport distribution function. For a Bloch electron system, $\Sigma(E)$ is defined by:

$$\Sigma(E) := \sum_{n=1}^{\infty} \sum_{\boldsymbol{k} \in \mathrm{BZ}} v_1(n,\boldsymbol{k})^2 \tau(n,\boldsymbol{k}) \delta(E - E_{n,\boldsymbol{k}}),$$

where n is the band index, $\boldsymbol{k}$ is the Bloch wave vector within the first Brillouin zone, $v_1(n,\boldsymbol{k})$ is the component of the group velocity in the direction of applied electric field, $\tau(n,\boldsymbol{k})$ is the relaxation time (or lifetime) of the Bloch state, and $E_{n,\boldsymbol{k}}$ is the energy eigenvalue, all specified by the band index n and wave vector $\boldsymbol{k}$.

For a nearly isotropic case, where the magnitude of the group velocity vector, $v(n,\boldsymbol{k}) := \sqrt{v_1(n,\boldsymbol{k})^2 + v_2(n,\boldsymbol{k})^2 + v_3(n,\boldsymbol{k})^2}$, and $\tau(n,\boldsymbol{k})$ can be approximated as functions of energy, the transport distribution function can be written as:

$$\Sigma(E) \approx \frac{1}{3} v(E)^2 \tau(E) N(E),$$

where $N(E) = \sum_{n=1}^{\infty} \sum_{\boldsymbol{k} \in \mathrm{BZ}} \delta(E - E_{n,\boldsymbol{k}})$ is the density of states. This approximation leads to the following formula for conductivity at sufficiently low temperatures:

$$\sigma \approx e^2 D(\mu) N(\mu).$$

where $D(E) = v(E)^2 \tau(E)/3$ represents the diffusivity of electrons at energy E. It is useful to assume that the diffusivity remains constant with respect to small shifts in the Fermi energy or chemical composition, i.e., $D(\mu) = D$ (constant). This so-called constant-diffusivity approximation has proved successful in fitting experimental data from thermoelectric measurements on periodic approximants [60–62]. If we extend this approximation to iQCs, the conductivities of the present four samples should be compared using $\sigma \propto N(\mu)$.

The present data show that $\sigma_{300\ \mathrm{K}}$ increases in the order of Samples Q_3, H_1, L_1, and H_2, suggesting that the density of states at the Fermi level increases correspondingly in the same order. Moreover, the carrier densities of the three PA samples appear to be at least three times higher than that of the quasicrystalline sample, Q_3. Note that Sample Q_3 with $\sigma_{300\ \mathrm{K}} \sim 200\ (\Omega\mathrm{cm})^{-1}$ is among the most resistive iQCs reported to date.

Table 1
The four samples that were used for the thermoelectric measurements, with a reference to the corresponding SEM image of each sample.

Sample name	Phase	Nominal composition	Density [gcm^{-3}]	SEM image
H_1	3/2 PA: cubic	$Al_{70}Pd_{21}W_1Fe_8$	5.237	Fig. 6(b)
L_1	3/2 PA: trigonal	$Al_{70}Pd_{21}W_1Fe_8$	5.172	Fig. 7(b), right
H_2	3/2 PA: cubic	$Al_{70}Pd_{21}W_2Fe_7$	5.293	SFig.2(b), right
Q_3	i-QC	$Al_{70}Pd_{21}W_3Fe_6$	5.381	Fig. 6(c)

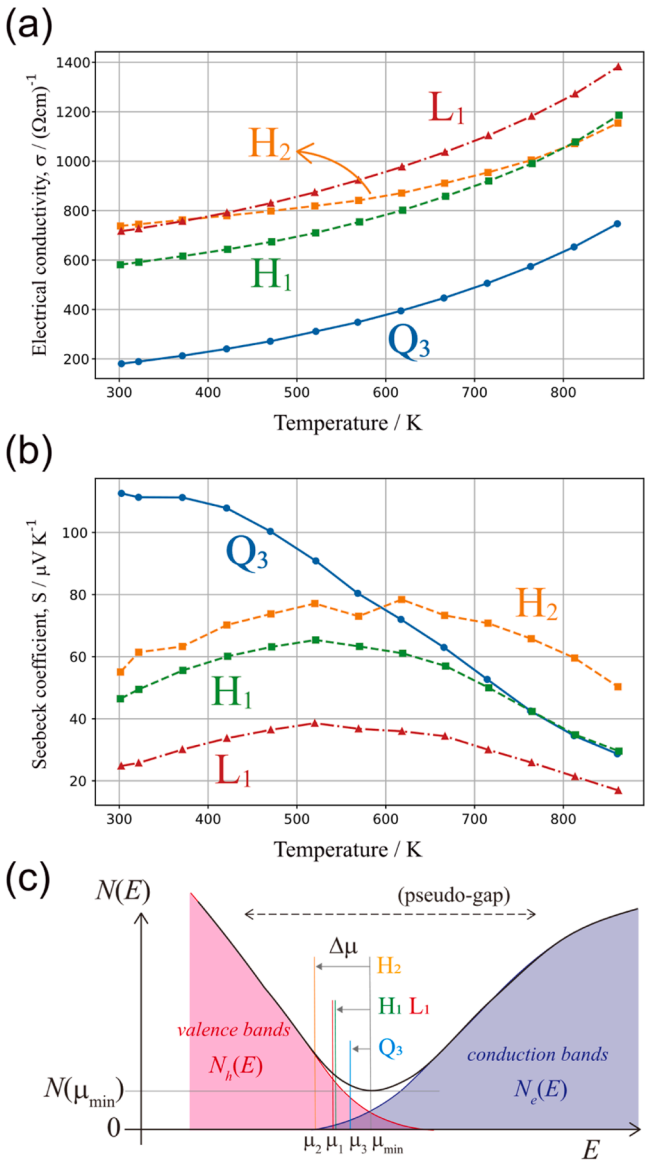

Fig. 8. (a and b) Temperature dependence of (a) the electrical conductivity σ and (b) the Seebeck coefficient S, for Samples Q_3 (blue), H_1 (green), L_1 (red), and H_2 (yellow). (c) A schematic illustration of the pseudogap with varying locations of the Fermi energy for the four samples. The total density of states, $N(E) = N_e(E) + N_h(E)$, is represented using a solid black line.

Meanwhile, the significantly smaller slope of the σ plot, compared to the other three samples, suggests that the increase of carrier excitation in Sample H_2 is modest by μ being away from the bottom of the pseudogap.

Fig. 8(b) presents the temperature dependence of the Seebeck coefficient (S). Based on the Mott formula [63],

$$S(\mu, T) = -\frac{\pi^2 {k_B}^2 T}{3|e|N(\mu)} \left(\frac{dN(E)}{dE} \right)_{E=\mu},$$

the positivity of S (especially at low temperatures) confirms that the first derivative $N'(\mu)$ is negative for all four samples. Since Samples Q_3, H_1, and L_1 exhibit similar slopes in their electrical conductivity plots, their first derivatives, $N'(\mu)$, are likely comparative. It follows that the Seebeck coefficients, S, at low temperatures are inversely proportional to $N(\mu)$, while the electrical conductivity, σ, is proportional to $N(\mu)$. However, despite Sample H_2 having the largest $N(\mu)$, as indicated by its highest electrical conductivity, σ, at 300 K and below, it still exhibits a higher Seebeck coefficient, S, than Samples H_1 and L_1. This is due to the exceptionally steep decay of $N(E)$ at $E = \mu$, which effectively enhances the ratio $|N'(\mu)|/N(\mu)$ for Sample H_2.

Fig. 8(b) also shows that the Seebeck coefficients, S, of the PA samples (H_1, L_1, H_2) display a broad maximum. The temperature T_{max}, at which the broad maximum of S occurs is roughly estimated as 523 K for Samples H_1 and L_1, and at around 623 K for Sample H_2. In contrast, the iQC sample (Q_3) exhibits a monotonic decrease with increasing temperature across the entire measured range; however, a broad maximum at $T_{max} \approx 300$ K may still be observed if the plot range is extended to lower temperatures.

Such a broad maximum in S may result from the so-called bipolar effect, arising from the competing contributions of valence and conduction bands, with holes and electrons as their respective charge carriers. In a simplified two-band picture, where it is assumed that holes and electrons contribute independently to the current density in response to either electric field or temperature gradient [64], the net electrical conductivity and Seebeck coefficient at temperature T can be expressed as

$$\sigma(\mu, T) = \sigma_h(\mu, T) + \sigma_e(\mu, T),$$

$$S(\mu, T) = \frac{\sigma_h(\mu, T) S_h(\mu, T) - \sigma_e(\mu, T) |S_e(\mu, T)|}{\sigma_h(\mu, T) + \sigma_e(\mu, T)},$$

where σ_x and S_x are, respectively, the partial conductivity and Seebeck coefficient associated with holes ($x = h$) or electrons ($x = e$).

The fact that S remains positive across the entire temperature range, as shown in Fig. 8(b), provides evidence that holes are the majority carriers, implying that the Fermi energy is located below the bottom of the pseudogap. However, as the temperature rises, electrons are excited as minority carriers, and their contribution to the conductivity becomes detrimental to the Seebeck coefficient. The distance of the Fermi energy, $\Delta\mu$, from the bottom of the pseudogap is essentially correlated with T_{max}. Since $T_{max} \approx 300$ K, which is the lowest among the four samples, the Fermi energy of the iQC sample is likely the closest to the bottom of the pseudogap. Conversely, the Fermi energy of Sample H_2, with $T_{max} \approx$ 623 K, is likely the farthest, while the remaining two samples, with $T_{max} \approx$ 523 K, are positioned in between. Fig. 8(c) schematically sketches the location of the Fermi energy within the pseudogap, as inferred from the present measurements, for all four samples.

Even though the valence electron concentration likely decreases with increasing the W content, the above results suggest that the Fermi energy of Sample Q_3 is closer to the bottom of the pseudogap compared to Sample H_2. This strongly indicates that the position and/or shape of the pseudogap has shifted slightly due to the structural transition from the 3/2 PA to the iQC, positioning the Fermi energy closer to the bottom of the pseudogap. Therefore, the structural change is likely driven by electronic factors [65].

In principle, the observed increase of $\sigma_{300\ K}$ in the order of Samples Q_3, H_1, L_1, and H_2 may reflect several factors: (i) *The position, depth, and width of the pseudogap*, which are largely determined by the kind and completeness of the structural order, as well as the orbital hybridization between Al *sp* and W *d*, which can be enhanced with increasing W content. (ii) *The relative position, $\Delta\mu$, of the Fermi energy measured from the bottom of the pseudogap*, which depends on the electron concentration. This may explain the increase of both $N(\mu)$ and $|N'(\mu)|$ for Sample H_2, for example. (iii) *The diffusivity (or mobility) of electrons at the Fermi energy*. Although we have assumed that all our samples have the same diffusivity D, the nature of electronic states still depends on structural details, including disorder, suggesting possible variations in D.

In general, all the above three factors can have sizeable effects on the transport properties. In particular, the contrast between H_1 and L_1 may be explained when the above three factors are taken into consideration. To gain further insights into their individual contributions, it would be useful to evaluate the electronic specific-heat coefficient from low-temperature specific-heat measurements as well as to perform spectroscopic studies (as in Ref. [48]) to probe the valence electronic structure more directly. Such studies will also provide valuable guidelines for fine-tuning the thermoelectric properties, potentially allowing us to design suitable materials for energy applications [66,67]. Our preliminary assessments on the thermoelectric performance (Supplementary Fig. 3) shows that Sample H_2 displaying the largest Seebeck coefficient at above 600 K exhibits the highest value of the dimensionless figure of merit, reaching $zT \sim 0.12$.

4. Concluding remarks

In the present study, the two kinds of 3/2 PAs, with cubic $2 \times 2 \times 2$ and trigonal superstructures, as well as the F-type iQC were identified as equilibrium phases in the Al-Pd-W-Fe system. All the alloy samples were synthesized using the nominal composition formula, $Al_{70}Pd_{21}W_xFe_{9-x}$, with $x = 0$ corresponding to C_1-AlPdFe. Both forms of the 3/2 PAs were found to reach equilibrium in alloys synthesized with $x = 1$ or $x = 2$ if annealing was performed at appropriate temperatures for an extended period. We observed that at $x = 1$, the C_1-phase impurity formed during the arc-melting process could be dissolved into the 3/2 PA only through extended annealing; however, it was more effectively eliminated at $x = 2$ due to the reduced Fe content. Alloys dominated by the F-type iQC were obtained at $x = 3$, though they often contained W-poor and W-rich components as minor impurities, which could still be suppressed through extended annealing. Furthermore, alloys synthesized with higher W contents (i.e., $x = 5$ and $x = 7$) exhibited a binary coexistence of a novel W-rich phase with a hexagonal crystal structure and a quaternary extension of ε-AlPdFe.

Note that our heuristic attempts to obtain high-quality monophase samples of the 3/2 PAs and F-type iQC provided an exceptional opportunity to explore the relationship between icosahedral orders and physical properties. The thermoelectric measurements of the four monophase samples, as presented in Section 3.4, provide clear evidence that the valence band structure, particularly the pseudogap near the Fermi level, varies with the structural and compositional changes. However, whether the enhanced hybridization between Al-*sp* and W-*d* orbitals, compared to that between Al-*sp* and Cr/Mo-*d* orbitals, leads to a deepening of the pseudogap remains a hypothesis that still needs verification.

There is no doubt that this work will stimulate further experimental studies on the pseudogap in similar complex compounds. Moreover, the results encourage us to revisit our previous systems, where Cr and Mo were used to replace Fe, to conduct more systematic assessments of different icosahedral orders and their implications for controlling physical properties. Such studies are expected to provide valuable guidelines for fine-tuning thermoelectric properties, potentially enhancing these materials for energy applications [66,67].

CRediT authorship contribution statement

Iwasaki Yutaka: Validation, Resources. **Fujita Nobuhisa:** Writing – review & editing, Writing – original draft, Visualization, Supervision, Funding acquisition, Conceptualization. **Ohhashi Satoshi:** Validation, Resources. **Takakura Hiroyuki:** Validation, Resources. **Aoyama Makito:** Visualization, Validation, Investigation.

Declaration of Generative AI and AI-assisted technologies in the writing process

During the preparation of the manuscript, the authors used ChatGPT to enhance readability and eliminate language errors. The final content was reviewed and edited by the authors as needed. The authors take full responsibility for the content of the published article.

Declaration of Competing Interest

The authors declare the following financial interests/personal relationships which may be considered as potential competing interests: Nobuhisa Fujita reports financial support was provided by Japan Society for the Promotion of Science. Nobuhisa Fujita reports financial support was provided by Japan Science and Technology Agency. If there are other authors, they declare that they have no known competing financial interests or personal relationships that could have appeared to influence the work reported in this paper.

Acknowledgement

This work was supported by Japan Society for the Promotion of Science through Grant-in-Aid for Scientific Research (Grant No. JP19H05819) and Japan Science and Technology Agency through CREST (Grant No. JPMJCR2203).

Appendix A. Supporting information

Supplementary data associated with this article can be found in the online version at doi:10.1016/j.jallcom.2025.178838.

Data availability

Data will be made available on request.

References

[1] D. Shechtman, I. Blech, D. Gratias, J.W. Cahn, Metalic Phase with Long-Range Orientational Order and No Traslational Symmetry, Phys. Rev. Lett. 53 (20) (1984) 1951–1953.
[2] D. Levine, P.J. Steinhardt, Quasicrystals: A New Class of Ordered Structures, Phys. Rev. Lett. 53 (26) (1984) 2477–2480.
[3] N. Fujita, M. Mihalkovič, C.L. Henley, Canonical-Cell Tilings and their Atomic Decorations, Isr. J. Chem. 64 (10-11) (2024) e202300130.
[4] Z. Stadnik, Physical Properties of Quasicrystals, Springer, Berlin, 1999.
[5] J. Hafner, M. Krajčí, Electronic structure of quasicrystalline Al–Zn–Mg alloys and related crystalline, amorphous, and liquid phases, Phys. Rev. B 47 (18) (1993) 11795–11809.
[6] U. Mizutani, Hume-Rothery Rules for Structurally Complex Alloy Phases, Taylor & Francis Group, CRC Press, 2011.
[7] A.P. Tsai, A test of Hume-Rothery rules for stable quasicrystals, J. Non-Cryst. Solids 334–335 (2004) 317–322.
[8] A.P. Tsai, Icosahedral clusters, icosaheral order and stability of quasicrystals—a view of metallurgy, Sci. Technol. Adv. Mater. 9 (1) (2008) 013008.
[9] M. Widom, D.P. Deng, C.L. Henley, Transfer-Matrix Analysis of a Two-Dimensional Quasicrystal, Phys. Rev. Lett. 63 (3) (1989) 310–313.
[10] K.J. Strandburg, L.-H. Tang, M.V. Jarić, Phason Elasticity in Entropic Quasicrystals, Phys. Rev. Lett. 63 (3) (1989) 314–317.
[11] M. de Boissieu, Stability of quasicrystals: energy, entropy and phason modes, Philos. Mag. 86 (6-8) (2006) 1115–1122.
[12] K. Deguchi, S. Matsukawa, N.K. Sato, T. Hattori, K. Ishida, H. Takakura, T. Ishimasa, Quantum critical state in a magnetic quasicrystal, Nat. Mater. 11 (12) (2012) 1013–1016.
[13] S. Watanabe, K. Miyake, Effects of crystalline electronic field and onsite interorbital interaction in Yb-based quasicrystal and approximant crystal, J. Phys.: Condens. Matter 30 (2018) 184001.
[14] K. Kamiya, T. Takeuchi, N. Kabeya, N. Wada, T. Ishimasa, A. Ochiai, K. Deguchi, K. Imura, N.K. Sato, Discovery of superconductivity in quasicrystal, Nat. Commun. 9 (1) (2018) 154.
[15] S. Sakai, N. Takemori, A. Koga, R. Arita, Superconductivity on a quasiperiodic lattice: Extended-to-localized crossover of Cooper pairs, Phys. Rev. B 95 (2) (2017) 024509.
[16] R. Tamura, A. Ishikawa, S. Suzuki, T. Kotajima, Y. Tanaka, T. Seki, N. Shibata, T. Yamada, T. Fujii, C.-W. Wang, M. Avdeev, K. Nawa, D. Okuyama, T.J. Sato, Experimental Observation of Long-Range Magnetic Order in Icosahedral Quasicrystals, J. Am. Chem. Soc. 143 (47) (2021) 19938–19944.
[17] A.I. Goldman, Magnetism in icosahedral quasicrystals: current status and open questions, Sci. Technol. Adv. Mater. 15 (2014) 044801.
[18] A.P. Tsai, J.Q. Guo, E. Abe, H. Takakura, T.J. Sato, A stable binary quasicrystal, Nature 408 (2000) 537–538.
[19] H. Takakura, C.P. Gómez, A. Yamamoto, M. De Boissieu, A.P. Tsai, Atomic structure of the binary icosahedral Yb–Cd quasicrystal, Nat. Mater. 6 (1) (2007) 58–63.
[20] A.I. Goldman, R.F. Kelton, Quasicrystals and crystalline approximants, Rev. Mod. Phys. 65 (1) (1993) 213–230.
[21] C.P. Gómez, S. Lidin, Comparative structural study of the disordered MCd_6 quasicrystal approximants, Phys. Rev. B 68 (2) (2003) 024203.
[22] C.P. Gómez, S. Lidin, Structure of $Ca_{13}Cd_{76}$: A Novel Approximant to the $MCd_{5.7}$ Quasicrystals (M=Ca, Yb), Angew. Chem. (Int. Ed.) 40 (21) (2001) 4037–4039.
[23] V. Elser, Indexing problems in quasicrystal diffraction, Phys. Rev. B 32 (8) (1985) 4892–4898.
[24] J.W. Cahn, D. Shechtman, D. Gratias, Indexing of icosahedral quasiperiodic crystals, J. Mater. Res. 1 (1) (1986) 13–26.
[25] A.L. Mackay, De nive quinquangula: On the pentagonal snowflake, Sov. Phys. Crystallogr. 26 (5) (1981) 517–522.
[26] P. Kramer, R. Neri, On periodic and non-periodic space fillings of E^m obtained by projection, Acta Cryst. A 40 (1984) 580–587.
[27] M. Duneau, A. Katz, Qnasiperiodic Patterns, Phys. Rev. Lett. 54 (25) (1985) 2688–2691.
[28] A.P. Tsai, A. Inoue, Y. Yokoyama, T. Masumoto, Stable Icosahedral Al–Pd–Mn and Al–Pd–Re Alloys, Mater. Trans. JIM 31 (2) (1990) 98–103.
[29] T. Asao, R. Tamura, S. Takeuchi, New stable icosahedral phases in Al–Pd–Ru and Al–Pd–Os systems, Philos. Mag. Lett. 82 (4) (2002) 217–223.
[30] J.-M. Dubois, So Useful, Those Quasicrystals, Isr. J. Chem. 51 (11–12) (2011) 1168–1175.
[31] J.-M. Dubois, Properties- and applications of quasicrystals and complex metallic alloys, Chem. Soc. Rev. 41 (20) (2012) 6760–6777.
[32] S. Balanetskyy, B. Grushko, E. Kowalska-Strzęciwilk, T.Y. Velikanova, K. Urban, An investigation of the Al–Pd–Fe phase diagram between 50 and 100 at% Al: phase equilibria at 900–1020°C, J. Alloy. Compd. 364 (1–2) (2004) 164–170.
[33] S. Balanetskyy, B. Grushko, T.Y. Velikanova, K. Urban, Investigation of the Al–Pd–Fe phase diagram between 50 and 100 at% Al: ternary phases, J. Alloy. Compd. 368 (1-2) (2004) 169–174.
[34] S. Balanetskyy, T.Y. Velikanova, B. Grushko, An investigation of the Al–Pd–Fe phase diagram between 50 and 100at% Al: reaction scheme, J. Alloy. Compd. 394 (1-2) (2005) 219–225.
[35] D. Pavlyuchkov, B. Grushko, T.Y. Velikanova, An investigation of the high-Al part of the Al–Pd–Ru phase diagram at 790–900 °C, J. Alloy. Compd. 469 (1–2) (2009) 146–151.
[36] B. Przepiórzyński, B. Grushko, M. Surowiec, An investigation of the Al–Pd–Rh phase diagram between 50 and 100at% Al, Intermetallics 14 (5) (2006) 498–504.
[37] D. Pavlyuchkov, B. Grushko, T.Y. Velikanova, An investigation of the Al–Pd–Ir phase diagram between 50 and 100at% Al, J. Alloy. Compd. 453 (1–2) (2008) 191–196.
[38] N. Fujita, H. Takano, A. Yamamoto, A.-P. Tsai, Cluster-packing geometry for Al-based F-type icosahedral alloys, Acta Crystallogr. Sect. A 69 (2013) 322–340.
[39] N. Fujita, M. Ogashiwa, A Unified Geometrical Framework for Face-Centered Icosahedral Approximants in Al–Pd–TM (TM = Transition Metal) Systems, Mater. Trans. 62 (3) (2021) 329–337.
[40] K. Sugiyama, N. Kaji, K. Hiraga, T. Ishimasa, Crystal structure of a cubic $Al_{70}Pd_{23}Mn_6Si$; a 2/1 rational approximant of an icosahedral phase, Z. Kristallogr. – Cryst. Mater. 213 (2) (1998) 90–95.
[41] C.L. Henley, Cell geometry for cluster-based quasicrystal models, Phys. Rev. B 43 (1) (1991) 993–1020.
[42] A.-P. Tsai, Discovery of stable icosahedral quasicrystals: progress in understanding structure and properties, Chem. Soc. Rev. 42 (2013) 5352–5365.
[43] T. Janssen, Crystallography of quasi-crystals, Acta Crystallogr. Sect. A 42 (4) (1986) 261–271.
[44] D.S. Rokhsar, N.D. Mermin, D.C. Wright, Rudimentary quasicrystallography: The icosahedral and decagonal reciprocal lattices, Phys. Rev. B 35 (11) (1987) 5487–5495.
[45] L.S. Levitov, J. Rhyner, Crystallography of quasicrystals; application to icosahedral symmetry, J. Phys. Fr. 49 (11) (1988) 1835–1849.
[46] V. Elser, C.L. Henley, Crystal and Quasicrystal Structures in Al–Mn–Si Alloys, Phys. Rev. Lett. 55 (26) (1985) 2883–2886.
[47] T. Yamada, H. Takakura, A. Yamamoto, Structure of face-centred icosahedral quasicrystals with cluster close packing, Acta Crystallogr. Sect. A 80 (6) (2024) 422–438.

[48] S. Sarkar, P. Sadhukhan, V.K. Singh, A. Gloskovskii, K. Deguchi, N. Fujita, S. R. Barman, Bulk electronic structure of high-order quaternary approximants, Phys. Rev. Res. 3 (1) (2021) 013151.
[49] T. Fujiwara, T. Yokokawa, Universal Pseudogap at the Fermi Energy in Quasicrystals, Phys. Rev. Lett. 66 (3) (1991) 333–336.
[50] U. Mizutani, H. Sato, T.B. Massalski, The original concepts of the Hume-Rothery rule extended to alloys and compounds whose bonding is metallic, ionic, or covalent, or a changing mixture of these, Prog. Mater. Sci. 120 (2021) 100719.
[51] M. Krajčí, J. Hafner, Topologically induced semiconductivity in icosahedral Al–Pd–Re and its approximants, Phys. Rev. B 75 (2) (2007) 024116.
[52] N.K. Mukhopadhyay, G.C. Weatherly, D.J. Lloyd, J.D. Embury, Synthesis and characterization of quasicrystals in an Al-Fe-W alloy, Scr. Metall. Mater. 27 (1) (1992) 111–116.
[53] A. Le Bail, H. Duroy, J.L. Fourquet, Ab-initio structure determination of $LiSbWO_6$ by X-ray powder diffraction, Mater. Res. Bull. 23 (3) (1988) 447–452.
[54] V. Petříček, L. Palatinus, J. Plášil, M. Dušek, $J_{ANA}2020$ – a new version of the crystallographic computing system J_{ANA}, Z. Kristallogr. – Cryst. Mater. 238 (7–8) (2023) 271–282.
[55] M. Boudard, H. Klein, M. de Boissieu, M. Audier, H. Vincent, Structure of quasicrystalline approximant phase in the Al–Pd–Mn system, Philos. Mag. A 74 (4) (1996) 939–956.
[56] E. Kirkendall, L. Thomassen, C. Upthegrove, Rates of diffusion of copper and zinc in alpha brass, Trans. AIME 133 (1939) 186–203.
[57] E.O. Kirkendall, Diffusion of zinc in alpha brass, Trans. AIME 147 (1942) 104–110.
[58] A.D. Smigelskas, E.O. Kirkendall, Zinc diffusion of alpha brass, Trans. AIME 171 (1947) 130–142.
[59] G.D. Mahan, J.O. Sofo, The best thermoelectric, Proc. Natl. Acad. Sci. USA 93 (1996) 7436–7439.
[60] Y. Iwasaki, K. Kitahara, K. Kimura, Experimental realization of a semiconducting quasicrystalline approximant in Al–Si–Ru system by band engineering, Phys. Rev. Mater. 3 (6) (2019) 061601(R).
[61] Y. Iwasaki, K. Kitahara, K. Kimura, Effects of Cu doping on thermoelectric properties of Al–Si–Ru semiconducting quasicrystalline approximant, Phys. Rev. Mater. 5 (2021) 125401.
[62] K. Kitahara, K. Kimura, Interband Contribution to Thermoelectric Properties of Al–Cu–Ir Quasicrystalline Approximant, Mater. Trans. 62 (2) (2021) 149–154.
[63] M. Jonson, G.D. Mahan, Mott's formula for the thermopower and the Wiedemann-Franz law, Phys. Rev. B 21 (10) (1980) 4223–4229.
[64] J. Drabble, H. Goldsmid, Thermal Conduction in Semiconductors, Pergamon Press, 1961.
[65] M. Krajčí, M. Windisch, J. Hafner, G. Kresse, M. Mihalkovič, Atomic and electronic structure of icosahedral Al–Pd–Mn alloys and approximant phases, Phys. Rev. B 51 (24) (1995) 17355–17378.
[66] E. Maciá Barber, Chemical Bonding and Physical Properties in Quasicrystals and Their Related Approximant Phases: Known Facts and Current Perspectives, Appl. Sci. 9 (10) (2019) 2132.
[67] Y. Takagiwa, K. Kimura, Metallic–covalent bonding conversion and thermoelectric properties of Al-based icosahedral quasicrystals and approximants, Sci. Technol. Adv. Mater. 15 (4) (2014) 044802.